



University of
Zurich^{UZH}

Zurich Open Repository and
Archive

University of Zurich
University Library
Strickhofstrasse 39
CH-8057 Zurich
www.zora.uzh.ch

Year: 2016

Promoting photochemical water oxidation with metallic band structures

Liu, Hongfei ; Moré, René ; Grundmann, Henrik ; Cui, Chunhua ; Erni, Rolf ; Patzke, Greta R

Abstract: The development of economic water oxidation catalysts is a key step toward large-scale water splitting. However, their current exploration remains empirical to a large extent. Elucidating the correlations between electronic properties and catalytic activity is crucial for deriving general and straightforward catalyst design principles. Herein, strongly correlated electronic systems with abundant and easily tunable electronic properties, namely $\text{La}_{1-x}\text{Sr}_x\text{BO}_3$ perovskites and $\text{La}_{2-x}\text{Sr}_x\text{BO}_4$ layered perovskites ($\text{B} = \text{Fe}, \text{Co}, \text{Ni}, \text{or Mn}$), were employed as model systems to identify favorable electronic structures for water oxidation. We established a direct correlation between the enhancement of catalytic activity and the insulator to metal transition through tuning the electronic properties of the target perovskite families via the $\text{La}^{3+}/\text{Sr}^{2+}$ ratio. Their improved photochemical water oxidation performance was clearly linked to the increasingly metallic character. These electronic structure–activity relations provide a promising guideline for constructing efficient water oxidation catalysts.

DOI: <https://doi.org/10.1021/jacs.5b10215>

Posted at the Zurich Open Repository and Archive, University of Zurich

ZORA URL: <https://doi.org/10.5167/uzh-132895>

Journal Article

Published Version

Originally published at:

Liu, Hongfei; Moré, René; Grundmann, Henrik; Cui, Chunhua; Erni, Rolf; Patzke, Greta R (2016). Promoting photochemical water oxidation with metallic band structures. *Journal of the American Chemical Society*, 138(5):1527-1535.

DOI: <https://doi.org/10.1021/jacs.5b10215>

Promoting Photochemical Water Oxidation with Metallic Band Structures

Hongfei Liu,[†] René Moré,[†] Henrik Grundmann,[‡] Chunhua Cui,[†] Rolf Erni,[§] and Greta R. Patzke^{*,†}

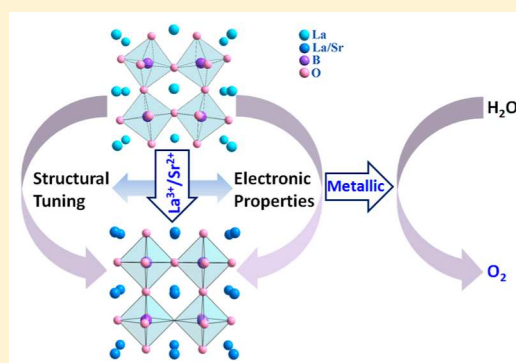
[†]Department of Chemistry, University of Zurich, Winterthurerstrasse 190, CH-8057 Zurich, Switzerland

[‡]Physics Institute, University of Zurich, Winterthurerstrasse 190, CH-8057 Zurich, Switzerland

[§]Electron Microscopy Center, Empa, Swiss Federal Laboratories for Materials Science and Technology, Überlandstrasse 129, CH-8600 Dübendorf, Switzerland

S Supporting Information

ABSTRACT: The development of economic water oxidation catalysts is a key step toward large-scale water splitting. However, their current exploration remains empirical to a large extent. Elucidating the correlations between electronic properties and catalytic activity is crucial for deriving general and straightforward catalyst design principles. Herein, strongly correlated electronic systems with abundant and easily tunable electronic properties, namely $\text{La}_{1-x}\text{Sr}_x\text{BO}_3$ perovskites and $\text{La}_{2-x}\text{Sr}_x\text{BO}_4$ layered perovskites ($\text{B} = \text{Fe}, \text{Co}, \text{Ni}, \text{or Mn}$), were employed as model systems to identify favorable electronic structures for water oxidation. We established a direct correlation between the enhancement of catalytic activity and the insulator to metal transition through tuning the electronic properties of the target perovskite families via the $\text{La}^{3+}/\text{Sr}^{2+}$ ratio. Their improved photochemical water oxidation performance was clearly linked to the increasingly metallic character. These electronic structure–activity relations provide a promising guideline for constructing efficient water oxidation catalysts.



INTRODUCTION

Visible-light driven water splitting is a promising strategy to directly convert solar energy into clean and storable hydrogen.^{1–4} One of the major challenges associated with its implementation on a large scale is the development of robust and economic catalyst to drive the kinetically demanding water oxidation half reaction.^{5,6} This has promoted the exploration of earth-abundant transition metal ($\text{Co}, \text{Fe}, \text{Mn}, \text{Ni}, \text{Cu}$, etc.) based compounds for both homogeneous^{7–11} and heterogeneous^{12–21} water oxidation catalysis.

Deeper insight into the four-electron transfer mechanism of water oxidation ($2\text{H}_2\text{O} \rightarrow \text{O}_2 + 4\text{H}^+ + 4\text{e}^-$) is requested to substantially promote the targeted design and synthesis of water oxidation catalysts (WOC).²² However, such mechanistic studies remain a great challenge so far, especially for heterogeneous systems. In contrast, optimization of materials performance via tuning of their electronic properties is a general strategy in catalysis (e.g., via doping, heterojunctions, structural tuning etc.). These approaches are now extended on oxide-related oxygen evolution/reduction catalysts for establishing activity-related electronic property descriptors, e.g., the oxidation states of the active metal centers,^{23–26} $\text{M}-\text{OH}$ bond strengths,²⁷ e_g electron configurations,²⁸ surface affinity to oxygen species,²⁹ and O p-band energy levels.³⁰

Currently, lithium battery materials such as LiMn_2O_4 ,^{31,32} LiCoO_2 ,^{14,33–35} LiCoPO_4 ,³⁶ and $\text{Li}_2\text{Mn}_2\text{P}_2\text{O}_7$ ³⁷ oxides are intensively studied for water oxidation, because their structure

and electronic properties (e.g., valence states of the active metal centers, surface electrophilicity, $\text{Co } 3\text{d}-\text{O } 2\text{p}$ hybridization, e_g configuration, and hole mobility) can be easily tailored through delithiation. Recently, we observed significant enhancement of water oxidation activities for both spinel-type and layered LiCoO_2 oxides after delithiation, and their enhanced activity was correlated to the improved charge carrier mobility.³⁸

On the way to general electronic properties–catalytic activity relations, catalytically active model systems with well-defined and easily tunable electronic structures are highly sought-after. Herein, we newly target strongly correlated electronic systems for photochemical water oxidation. Perovskite or layered perovskite oxides containing $\text{Fe}, \text{Co}, \text{Mn}$, and Ni transition metal centers are known as typical strongly correlated electron systems featuring strong Coulomb repulsion between the 3d electrons, which entails various electronic phenomena, such as orbital ordering and electron localization.³⁹ The title compounds excel through facile options to tune their charge transport and magnetic properties through modifying the 3d electronic interactions as a function of temperature, pressure, magnetic/electrical fields, or composition. This has given rise to manifold interesting physical properties, such as metal to insulator transitions, high temperature superconductivity and colossal magnetoresistance. Nevertheless, the electronic proper-

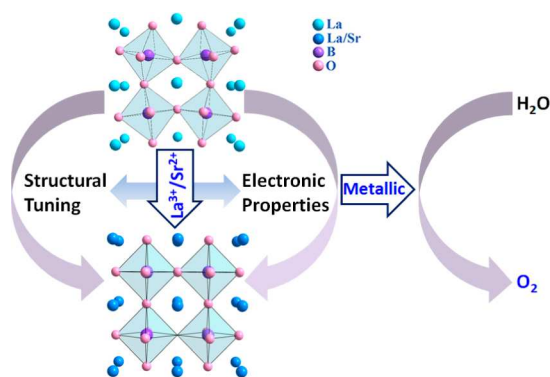
Received: September 29, 2015

Published: January 15, 2016

ties underlying these physical properties remain widely unexplored for catalysis to date. In principle, these charge transport and magnetic properties may potentially affect the catalytic efficiency,⁴⁰ especially for photochemical reactions⁴¹ involving charge transfer processes.

Many perovskite-type compounds are among today's most prominent materials with versatile applications, e.g., in catalysts, superconductors, data storage media, gas sensors, solar cells, or solid oxide fuel cells, due to their outstanding structural and compositional flexibility.^{42–46} ABO₃-type perovskite oxides contain alkaline-earth or lanthanide cations on the A site and tri- or tetravalent transition metal cations on the B site. The 3D network of corner-sharing BO₆ octahedra (Scheme 1) lends the

Scheme 1. Tuning the Electronic Properties of La_{1-x}Sr_xBO₃ and La_{2-x}Sr_xBO₄ (B = Fe, Co, Mn, or Ni; A = La and Sr) via the La³⁺/Sr²⁺ Ratio for Photochemical Water Oxidation



perovskite motif considerable flexibility for compositional variations entailing structural distortions. Introduction of heteroatoms on the A or B sites can lead to valence state changes and structural adjustments (e.g., B—O bond length and B—O—B angle, cf. Scheme 1) which can modify the electronic properties⁴⁷ through influencing the interactions between the 3d electrons of the B site atoms.

In the following, we explore the flexible electronic properties of strongly correlated electron systems, i.e., La_{1-x}Sr_xBO₃ and La_{2-x}Sr_xBO₄ (B = Fe, Co, Mn, or Ni; A = La and Sr), for photochemical water oxidation. Through tuning their electronic structure via the La³⁺/Sr²⁺ ratio on the A site and tracking the water oxidation performance, we link the enhanced catalytic activity directly to the emerging metallic character.

RESULTS AND DISCUSSION

We started from La_{1-x}Sr_xFeO₃ (A = La and Sr, B = Fe), because the title compound series can accommodate the entire Sr content range from $x = 0$ to 1. Formation of phase pure perovskite structures of La_{1-x}Sr_xFeO₃ ($x = 0, 0.25, 0.5, 0.75$, and 1) was verified through matching of their powder X-ray diffraction (PXRD) patterns with the standard pattern of LaFeO₃ (JCPDS card No. 37–1943, cf. Figure 1). Increasing Sr contents lead to a gradual structural transition from orthorhombic ($0 \leq x \leq 0.2$) via rhombohedral ($0.4 \leq x \leq 0.7$) to cubic ($0.8 \leq x \leq 1.0$) symmetry.⁴⁸ This structural adjustment is also evident from a peak shift toward higher angles (cf. (240) reflection in Figure 1), as well as from the gradual disappearance of the (101) reflection and the appearance of (111) reflections (Figure S1).

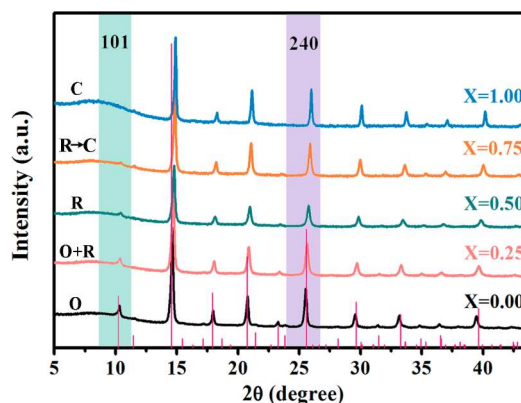


Figure 1. PXRD patterns of La_{1-x}Sr_xFeO₃ (MoK α_1 radiation; bottom: standard pattern of LaFeO₃ (JCPDS card No. 37–1943). Structural transitions are labeled as follows: O (orthorhombic, *Pnma*), R (rhombohedral, *R3c*), and C (cubic, *Pm-3m*), respectively.

The photochemical water oxidation activity of La_{1-x}Sr_xFeO₃ was evaluated according to a standard protocol using [Ru(bpy)₃]²⁺ as photosensitizer and S₂O₈²⁻ as sacrificial electron acceptor. The produced oxygen in solution was online monitored with a Clark electrode (Figure 2a), while the oxygen diffused to the headspace was detected by GC (Figure S3). Comparably low oxygen amounts (below 50 $\mu\text{mol L}^{-1}$) evolved from the first three samples with $x \leq 0.5$. A further increase of the Sr²⁺ content resulted in significant improvement of the corresponding water oxidation activities, and equilibrium oxygen concentrations of 286 and 615 $\mu\text{mol/L}$ were achieved for La_{0.25}Sr_{0.75}FeO₃ and SrFeO₃, respectively. GC detection of oxygen in the headspace further confirmed this trend. TOF values were calculated based on the initial 50 s irradiation before significant oxygen diffused to the headspace. A sharp TOF increase set in from $x = 0.75$, and the maximum TOF observed for SrFeO₃ is 2.4×10^{-3} per sec per iron which is 16.5 times higher than that of LaFeO₃ (Figure 2b). Comparison to the reported TOF values of binary iron oxides shows that SrFeO₃ can outperform them in the [Ru(bpy)₃]²⁺/S₂O₈²⁻ standard assay (Table S1). However, it should be emphasized that absolute performances are difficult to compare between different studies as the applied protocols⁴⁹ or even the specific test conditions used for the same protocol can significantly influence the catalytic activities.

Importantly, substantial improvement of the water oxidation performance was observed from $x = 0.75$ to 1, i.e., corresponding to the composition range where the cubic perovskite was formed. In the course of this structural adjustment, increased Fe valence states, shortened Fe—O bond lengths and straightened Fe—O—Fe bond angles (closer to 180°) generally lead to an insulator to metal transition, as evident from FT-IR spectra (Figure 2c). The disappearance of characteristic Fe—O stretching vibrations around 560 cm^{-1} for both La_{0.25}Sr_{0.75}FeO₃ and SrFeO₃ indicates the emergence of metallic properties with strong reflectivity toward infrared light.⁵⁰ Noteworthy, this electronic structure transition goes hand in hand with the improvement of water oxidation activity for $x \geq 0.75$. To clarify their possible correlation, the electronic properties of La_{1-x}Sr_xFeO₃ are subjected to a comprehensive analysis in the following.

X-ray absorption near edge spectra (XANES) were recorded at the Fe K-edge to trace the electronic structure changes as a function of Sr²⁺ content. A pre-edge absorption peak (orange

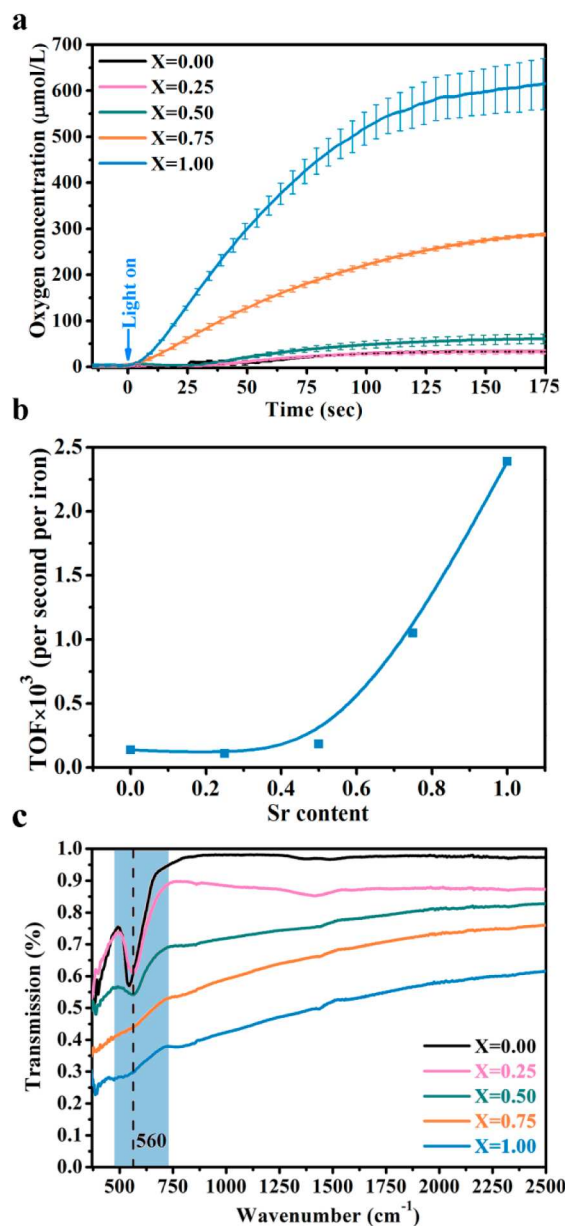


Figure 2. (a) Oxygen evolution during photochemical water oxidation with $\text{La}_{1-x}\text{Sr}_x\text{FeO}_3$ (oxygen was monitored online by a calibrated Clark electrode in solution, the error bars were estimated based on water oxidation tests in triplicate: 4 mg $\text{La}_{1-x}\text{Sr}_x\text{FeO}_3$, 5.25 mM $\text{Na}_2\text{S}_2\text{O}_8$ and 1.33 mM $[\text{Ru}(\text{bpy})_3]^{2+}$ were dispersed in 8 mL of 0.05 M phosphate buffer (pH 7), irradiation: 460 nm LED (5000 lx)), (b) TOF trend as a function of the Sr content (TOF values were calculated based on the initial 50 s irradiation before significant oxygen diffused to headspace), and (c) insulator to metal transition monitored by FT-IR spectroscopy at room temperature.

area in Figure 3a, enlarged in Figure 3b) at 7117 eV is assigned to the quadrupole-allowed $1s \rightarrow 3d$ transitions. The increasing absorption intensity of this peak with higher Sr contents is a characteristic indication for an increasing hole concentration in the Fe 3d bands. Furthermore, the saturation effect observed at $x \geq 0.75$ is consistent with the disappearance of the characteristic IR absorption bands at 560 cm^{-1} for $\text{La}_{0.25}\text{Sr}_{0.75}\text{FeO}_3$ and SrFeO_3 and points to the presence of less strongly bound charge carriers.⁵¹

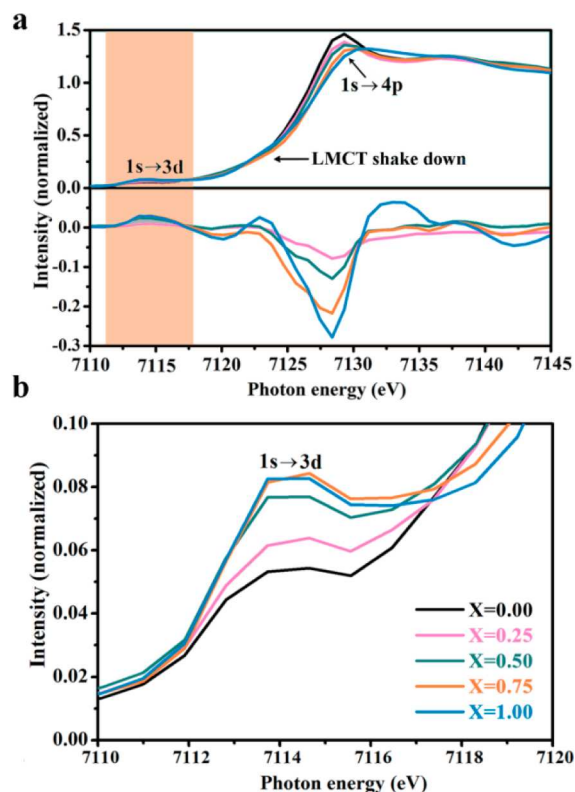


Figure 3. (a) Fe K-edge X-ray absorption spectra of $\text{La}_{1-x}\text{Sr}_x\text{FeO}_3$, and (b) zoom into the $1s$ to $3d$ transition absorption. The bottom section of (a) displays the absorption intensity difference of $\text{La}_{1-x}\text{Sr}_x\text{FeO}_3$ ($x = 0.25, 0.5, 0.75, 1.00$) relative to LaFeO_3 .

The absorption maximum arising from dipole-allowed $1s$ to $4p$ transitions continuously decreases with increasing Sr content (cf. absorption intensity difference relative to LaFeO_3 spectrum in Figure 3a (bottom)). This trend corresponds to the gradual formation of a metallic band structure with delocalized electrons and increasingly covalent Fe—O bonds.⁵¹ In contrast to $\text{La}_{0.25}\text{Sr}_{0.75}\text{FeO}_3$, SrFeO_3 exhibits a more significant broadening of the $1s \rightarrow 4p$ peak (Figure 3a) together with a ligand-to-metal charge transfer band (around 7123 eV, Figure S2). This provides further evidence for increasingly metallic properties of SrFeO_3 , giving rise to its superior water oxidation activity compared to $\text{La}_{0.25}\text{Sr}_{0.75}\text{FeO}_3$.

Fe K-edge extended X-ray absorption fine structure provides detailed information about the local structure around the Fe atoms (cf. Fourier transforms in Figure 4a). The first peak represents the interaction between Fe and first shell of oxygen atoms. A continuous decrease of the peak intensity goes hand in hand with a peak shift from $R = 1.53\text{--}1.47 \text{ \AA}$ when x increases from 0 to 0.5. For $x \geq 0.75$, both peak intensity and positions remain nearly constant, analogous to the saturation effect observed for the intensity of the $1s$ to $3d$ transitions. The Fe—O bond lengths derived from the R value of the first peak (Figure 4b) match well with the Rietveld refinement results (Table S4). The continuous decrease of Fe—O bond lengths from $x = 0$ to 0.75 indicates the gradual oxidation of Fe^{3+} to Fe^{4+} and increasingly covalent Fe—O bonds. The constant Fe—O distance trend from $x = 0.75$ to 1.00 is most likely due to the rhombohedral to cubic symmetry transition.

While previous works proposed a strong influence of the valence states of active metal centers on the water oxidation activity,^{23–25,52} the present catalytic results cannot be solely

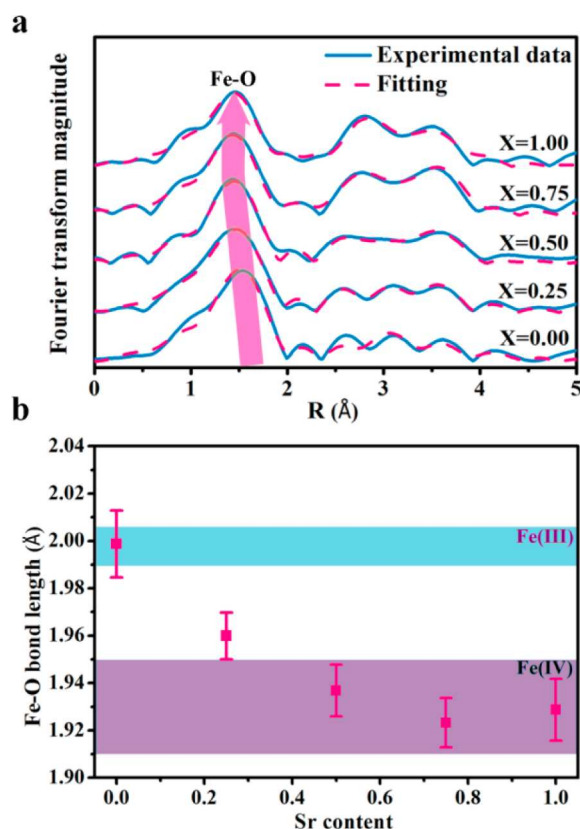


Figure 4. (a) Fit of the extended X-ray absorption fine structure of $\text{La}_{1-x}\text{Sr}_x\text{FeO}_3$ against the perovskite structure, and (b) resulting Fe—O bond lengths. The green and purple areas in (b) represent literature Fe—O bond length ranges for Fe(III) and Fe(IV), respectively.⁵¹

explained with the iron valence state changes: $\text{La}_{0.5}\text{Sr}_{0.5}\text{FeO}_3$ and $\text{La}_{0.25}\text{Sr}_{0.75}\text{FeO}_3$ with higher Fe valence states than LaFeO_3 do not exhibit notably higher water oxidation activities (Figure 2a).

The electronic structure transitions are also evident from a remarkable change of the surface affinity to oxygen species (Figure 5). O 1s spectra for $\text{La}_{1-x}\text{Sr}_x\text{FeO}_3$ are composed of two major peaks corresponding to lattice oxygen (~ 528.7 eV) and to surface absorbed oxygen species (~ 531.7 eV), respectively. Importantly, a significant reverse of the proportions of these two peaks sets in for $x \geq 0.75$. Furthermore, both $\text{La}_{0.25}\text{Sr}_{0.75}\text{FeO}_3$ and SrFeO_3 exhibit slight peak shifts compared to $\text{La}_{1-x}\text{Sr}_x\text{FeO}_3$ perovskites with lower Sr contents ($x = 0, 0.25$, and 0.5), namely lattice oxygen peaks at ca. 0.3 eV lower and surface oxygen peaks around 0.2 eV higher binding energies. The enrichment of surface oxygen species after the insulator to metal transition is consistent with the theoretically predicted stabilizing effect of metallic band structures on surface oxygen species.⁵³

The XPS valence band spectra mainly consist of the Fe 3d and O 2p states which cannot be well resolved into their respective features (Figure S9). Increasing the Sr content leads to decreased intensity of the Fe 3d state at around 2–4 eV and a more prominent O 2p state from 5 to 7 eV. However, for $x \geq 0.75$, the O 2p states become more distinct, and the intensity of the two shakeup satellites at around 10 and 12.5 eV increases. These strong satellite features were also observed on previously reported SrFeO_3 ⁵⁴ and other highly correlated metallic oxides, such as high- T_c superconducting copper oxides.⁵⁵

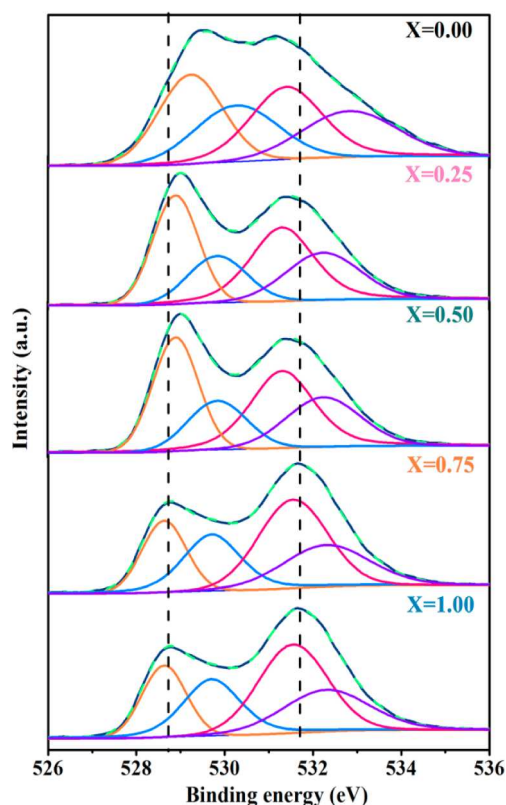


Figure 5. O 1s XPS spectra of $\text{La}_{1-x}\text{Sr}_x\text{FeO}_3$ (dashed lines around 528.7 and 531.7 eV represent lattice oxygen and surface absorbed oxygen species, respectively).

In line with a previous study,⁵⁶ temperature-dependent susceptibility measurements (Figure 6) indicate that both

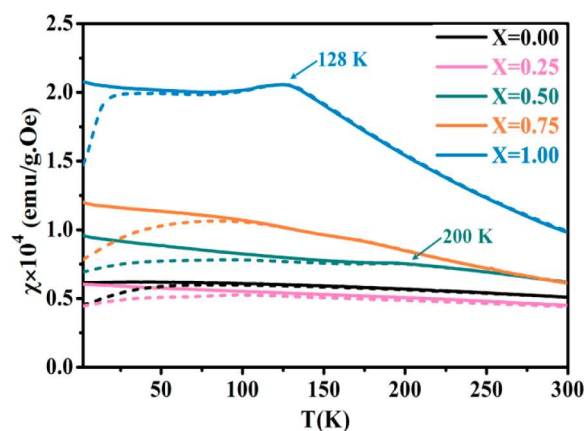


Figure 6. Temperature-dependent magnetic susceptibility of $\text{La}_{1-x}\text{Sr}_x\text{FeO}_3$ measured from 2 to 300 K (solid line: field cooling; dashed line: zero field cooling).

LaFeO_3 and $\text{La}_{0.75}\text{Sr}_{0.25}\text{FeO}_3$ are nearly antiferromagnetic over 2–300 K range, while $\text{La}_{0.5}\text{Sr}_{0.5}\text{FeO}_3$ experiences a slight ferromagnetic to antiferromagnetic transition around 200 K (Néel temperature). In contrast, SrFeO_3 displays a sharp ferromagnetic to antiferromagnetic transition at 128 K, which indicates a clearly defined electronic state (i.e., purely metallic before the ferromagnetic to antiferromagnetic transition). $\text{La}_{0.25}\text{Sr}_{0.75}\text{FeO}_3$ exhibits a complex magnetic behavior located in-between SrFeO_3 and $\text{La}_{0.5}\text{Sr}_{0.5}\text{FeO}_3$, thus implying an

intermediate electronic state giving rise to room temperature magnetic behavior between ferromagnetic and antiferromagnetic properties. The broad Néel transition temperature range from 120 to 175 K is either due to the complex electronic structure of $\text{La}_{0.5}\text{Sr}_{0.5}\text{FeO}_3$ or associated with a phase transition from cubic to rhombohedral.⁵⁷ The partially metallic character of $\text{La}_{0.25}\text{Sr}_{0.75}\text{FeO}_3$ at room temperature is consistent with its notably lower water oxidation activity compared to SrFeO_3 .

Moreover, the slightly higher magnetic moment (2–300 K range) of $\text{La}_{0.5}\text{Sr}_{0.5}\text{FeO}_3$ compared to LaFeO_3 and $\text{La}_{0.75}\text{Sr}_{0.25}\text{FeO}_3$ corresponds well with its significantly weaker FT-IR absorption band at 560 cm^{-1} as well as marginally higher oxygen evolution activity, indicating the onset of the insulator to metal transition. Noteworthy, the metallic properties are strongly related to the presence of ferromagnetism which facilitates 3d electron delocalization through double exchange effects. Furthermore, ferromagnetic centers may also act as stronger binding sites for triplet oxygen molecules, thereby accounting for the increased affinity of the metallic compounds to surface oxygen species. Thus, a clear correlation between ferromagnetism, metallic properties and water oxidation activity can be established.

Recent studies revealed that some oxide-type WOCs can undergo surface amorphization and compositional changes after electrochemical water oxidation.^{35,58} Therefore, we examined the morphology and composition of SrFeO_3 (the most active WOC among the $\text{La}_{1-x}\text{Sr}_x\text{FeO}_3$ series) by HR-TEM and EDXS analyses, respectively (Figure 7). Comparison of the representative HR-TEM images of SrFeO_3 before (Figure 7a) and after (Figure 7d) photochemical water oxidation clearly shows that no significant morphology changes occurred.

EDXS analyses of both particle surface and bulk compositions indicate a nearly constant intensity ratio of 1.2–1.3 between the Sr L and Fe K peaks of SrFeO_3 both before (Figures 7b,c) and after (Figures 7e and f) photochemical water oxidation. Furthermore, linear EDXS mapping across a SrFeO_3 nanoparticle after water oxidation (Figure S10) reveals a constant Sr L/Fe K ratio around 1.3 as well. These results indicate that Sr and Fe remain evenly distributed throughout the entire particles, in contrast to $\text{Ba}_{0.5}\text{Sr}_{0.5}\text{Co}_{0.8}\text{Fe}_{0.2}\text{O}_3$ which exhibits significant surface Ba^{2+} and Sr^{2+} leaching and amorphization after electrochemical water oxidation.⁵⁹

Furthermore, the concentrations of Sr and Fe ions in solution after photochemical water oxidation with SrFeO_3 were analyzed by ICP-MS, and minor amounts of dissolved Sr and Fe ions were detected (Table S3). Interestingly, this leaching-related phenomenon was also observed even after reference aging tests with SrFeO_3 in standard $[\text{Ru}(\text{bpy})_3]^{2+}/\text{S}_2\text{O}_8^{2-}$ photochemical water oxidation media without light irradiation. Comparable amounts of both Sr and Fe were detected in solutions after photochemical water oxidation and dark aging, respectively. This implies that the observed leaching phenomena are not caused by the water oxidation process. Our previous study on LiCoO_2 demonstrated that leaching of redox-inert Li^+ cations can influence its photochemical water oxidation activity.³⁸ However, Sr losses in the present materials are much lower compared to the extent of Li leaching from LiCoO_2 , because the significantly smaller Li^+ ions are much more mobile in this battery material.³⁸

$\text{La}_{1-x}\text{Sr}_x\text{CoO}_3$ perovskites as another typical strongly correlated electronic system were studied for comparison here. They exhibit an insulator to metal transition point at $x \approx$

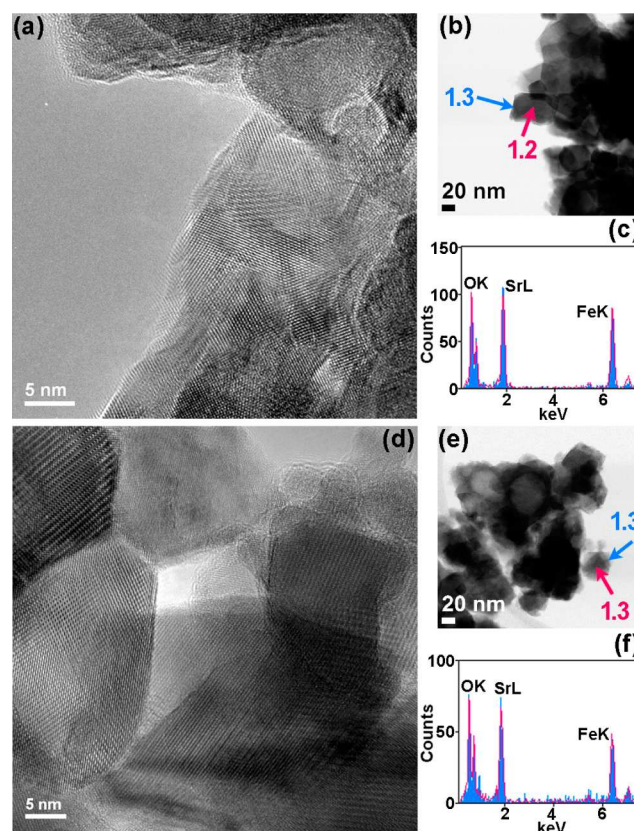


Figure 7. High resolution TEM images and EDXS spectra of SrFeO_3 before and after photochemical water oxidation: HR-TEM images before (a) and after (d) photochemical water oxidation; particle surface and bulk points for EDXS analysis before (b) and after (e) photochemical water oxidation; EDXS spectra before (c) and after (f) photochemical water oxidation (blue and red: surface and bulk analyses, respectively).

0.2⁶⁰ and show similar trends to $\text{La}_{1-x}\text{Sr}_x\text{FeO}_3$ with respect to both water oxidation activities and electronic structure evolution (Figure 8).

While the insulating LaCoO_3 displays two characteristic IR absorption bands (Figure 8b) at around 400 cm^{-1} and $500\text{--}600\text{ cm}^{-1}$ arising from O—Co—O bending and Co—O stretching vibrations,⁶¹ metallic $\text{La}_{0.8}\text{Sr}_{0.2}\text{CoO}_3$ exhibits no absorption at around 400 cm^{-1} and a much weaker absorption band in the $500\text{--}600\text{ cm}^{-1}$ range.

Further incorporation of Sr^{2+} only results in a slightly stronger background reflection for $\text{La}_{0.6}\text{Sr}_{0.4}\text{CoO}_3$ in the $380\text{--}1000\text{ cm}^{-1}$ region, which corresponds well with the minor increase of metallic properties beyond $x = 0.2$.⁶² The insulator to metal transition at $x = 0.2$ goes hand in hand with a significantly enhanced oxygen evolution for $\text{La}_{0.8}\text{Sr}_{0.2}\text{CoO}_3$ compared to LaCoO_3 (Figure 8a). Temperature-dependent magnetic susceptibility measurements indicate that LaCoO_3 is slightly paramagnetic (Figure 8c) with most Co^{3+} centers in low spin states (LS: $t_{2g}^6 e_g^0$). The insulator to metal transition at $x = 0.2$ is clearly reflected by a para- to ferromagnetic transition at around 240 K (cf. inflection points in the upper curves of Figure 8c). A further increase of the Sr content to 0.4 results in marginally increased magnetism, which matches well with the trends of both FT-IR spectra and water oxidation performance.

A slight shift of the Co 2p XPS peak toward higher binding energy after Sr^{2+} doping (Figure S12) indicates the partial oxidation of Co^{3+} to Co^{4+} which goes hand in hand with hole

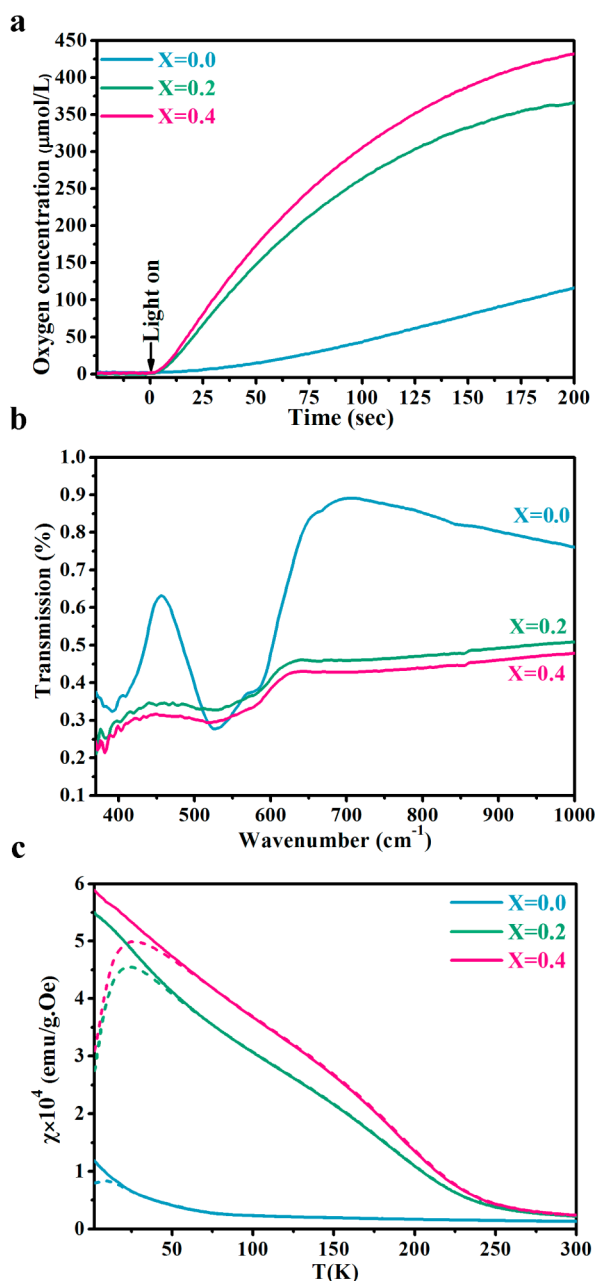


Figure 8. $\text{La}_{1-x}\text{Sr}_x\text{CoO}_3$ as photochemical water oxidation catalyst: (a) Photochemical oxygen evolution monitored online by a calibrated Clark electrode in solution (catalytic tests: 10 mg $\text{La}_{1-x}\text{Sr}_x\text{CoO}_3$, 26.25 mM $\text{Na}_2\text{S}_2\text{O}_8$, and 1.33 mM $[\text{Ru}(\text{bpy})_3]^{2+}$ were dispersed in 8 mL of 0.1 M phosphate buffer (pH 7); irradiation: 460 nm LED (5000 lx)); (b) insulator to metal transition monitored by FT-IR spectroscopy at room temperature; (c) temperature-dependent susceptibility measured from 2 to 300 K (solid line: field cooling; dashed line: zero field cooling).

doping in the Co 3d bands. This is in line with the increased amount of paramagnetic centers observed in temperature-dependent susceptibility measurements (Figure 8c). O 1s spectra of $\text{La}_{1-x}\text{Sr}_x\text{CoO}_3$ (Figure S11) display a very similar trend to $\text{La}_{1-x}\text{Sr}_x\text{FeO}_3$ in the course of the electronic structure transition. While the lattice oxygen peak (~ 529 eV) intensity of insulating LaCoO_3 is higher compared to adsorbed oxygen species (~ 531.5 eV), this ratio is completely inverted for the metallic compounds $\text{La}_{0.8}\text{Sr}_{0.2}\text{CoO}_3$ and $\text{La}_{0.6}\text{Sr}_{0.4}\text{CoO}_3$.

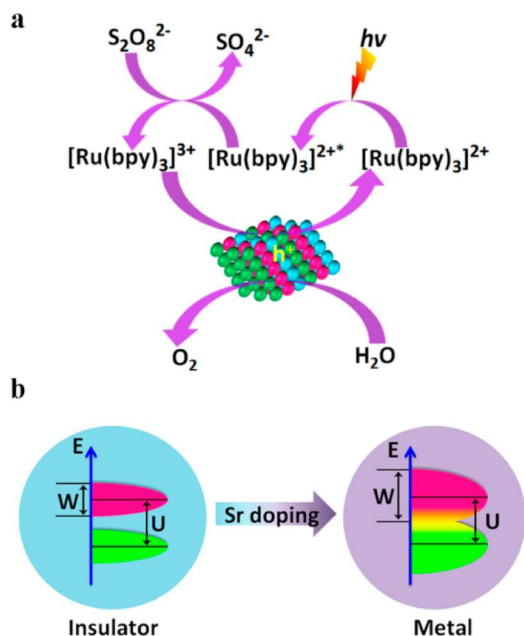
In following, we further investigated the electrochemical performance of $\text{La}_{1-x}\text{Sr}_x\text{CoO}_3$ compounds. In contrast to photochemical water oxidation, the influence of the Sr content on the electrochemical performance of $\text{La}_{1-x}\text{Sr}_x\text{CoO}_3$ is not comparably significant (Figure S23). Most likely, catalytic activities under electro- and photochemical conditions are limited by different factors. Indeed, a recent key study on manganese oxides⁴⁹ revealed different activity trends under photochemical ($[\text{Ru}(\text{bpy})_3]^{2+}/\text{S}_2\text{O}_8^{2-}$), chemical ($(\text{NH}_4)_2[\text{Ce}(\text{NO}_3)_6]$ as oxidant) and electrochemical water oxidation conditions. The anodic bias applied in electrochemical water oxidation is expected to facilitate the charge transfer across the bulk catalyst. Additionally, in situ XAS studies of manganese oxides⁶³ and amorphous cobalt oxide^{64,65} electrocatalysts demonstrated that their metal centers undergo a bulk valence change. Electrochemical methods thus modify the electronic properties or even the structural properties⁵⁸ of the investigated compounds in situ. The oxidation of Co^{3+} to Co^{4+} in the bulk of LaCoO_3 under electrochemical conditions may play an analogous role to Sr doping of LaCoO_3 , thereby accounting for the comparable electrochemical water oxidation activity trends between both $\text{La}_{1-x}\text{Sr}_x\text{CoO}_3$ series. Moreover, the realignment of the band structure under the applied bias may also change the interface electron transfer rate.

$\text{La}_{1-x}\text{Sr}_x\text{MnO}_3$ provides further evidence for the correlation between electronic structure and water oxidation activity. Both water oxidation activity trends (Figure S13a) and FT-IR spectra (Figure S13c) match well with the transition from paramagnetic insulator ($0 \leq x < 0.2$) to ferromagnetic metal ($0.2 \leq x < 0.5$) which is reverted into a paramagnetic insulator at higher Sr contents ($x \geq 0.5$).⁶⁶ The O 1s XPS spectra (Figure S13b) of $\text{La}_{1-x}\text{Sr}_x\text{MnO}_3$ display the expected proportional intensity increase of the signal related to surface oxygen species after the insulator to metal transition. However, it is far less significant compared to $\text{La}_{1-x}\text{Sr}_x\text{CoO}_3$ and $\text{La}_{1-x}\text{Sr}_x\text{FeO}_3$. This is likely due to the less pronounced metallic character of $\text{La}_{0.8}\text{Sr}_{0.2}\text{MnO}_3$, as evident from a strong remnant FT-IR absorption band at around 563 cm^{-1} .

Layered A_2BO_4 ($\text{B} = \text{Ni}, \text{Co}$) perovskites were studied for comparison as well. They exhibit a similar structural motif with insertion of an additional AO layer between the layers of $\{\text{BO}_6\}$ octahedra, giving rise to characteristic A_2BO_4 stoichiometries (Figure S14). In contrast to the ABO_3 perovskites with a 3D $\{\text{BO}_6\}$ network, the metallic properties of layered perovskites are dimensionally restricted to the corner-sharing $\{\text{BO}_6\}$ layers due to their separation by the insulating AO layers. Consequently, the observed improvement of water oxidation activity for $\text{La}_{2-x}\text{Sr}_x\text{NiO}_4$ (Figure S15a) and $\text{La}_{2-x}\text{Sr}_x\text{CoO}_4$ (Figure S16a) upon Sr^{2+} doping is less significant compared to $\text{La}_{1-x}\text{Sr}_x\text{CoO}_3$, $\text{La}_{1-x}\text{Sr}_x\text{FeO}_3$, and $\text{La}_{1-x}\text{Sr}_x\text{MnO}_3$.

Generally, photochemical water oxidation with the standard $[\text{Ru}(\text{bpy})_3]^{2+}$ /persulfate protocol proceeds via four basic steps (Scheme 2a): (1) excitation of $[\text{Ru}(\text{bpy})_3]^{2+}$ at around 460 nm; (2) oxidative quenching of excited $[\text{Ru}(\text{bpy})_3]^{2+*}$ by persulfate to form $[\text{Ru}(\text{bpy})_3]^{3+}$; (3) hole (h^+) injection from $[\text{Ru}(\text{bpy})_3]^{3+}$ into the WOC and regeneration of $[\text{Ru}(\text{bpy})_3]^{2+}$; (4) hole accumulation and transport by the WOC for subsequent water oxidation. Although the detailed steps of water oxidation mechanisms remain under intense investigation, the basic role of the oxide-type WOC in the process is well-defined: (a) collection and transport of the oxidative equivalents from single-electron $[\text{Ru}(\text{bpy})_3]^{3+}$ oxidants to the catalytically active centers; (b) transfer of the cumulated oxidative equivalents to

Scheme 2. Influence of the Insulator to Metal Transition on the Photochemical Water Oxidation Activity in Strongly Correlated Electronic Systems^a



^a(a) Photochemical water oxidation cycles with $[\text{Ru}(\text{bpy})_3]^{3+}$ as photosensitizer and persulfate as electron acceptor; (b) band structure evolution upon insulator to metal transition.

both molecular water and intermediate species related to oxygen evolution, as well as (c) facilitation of O—O bond formation.

In this study, we provide substantial evidence for a correlation between the insulator to metal transition and the enhancement of water oxidation activity. LaMO_3 and La_2MO_4 ($M = \text{Co}, \text{Fe}, \text{Mn}, \text{or Ni}$) are known as Mott insulators with strong Coulomb repulsion between the 3d electrons of the M metal centers which results in an energy gap (denoted as U in Scheme 2b) and renders the 3d electrons strongly localized. Hole doping by $\text{La}^{3+}/\text{Sr}^{2+}$ substitution broadens the bandwidth W of the 3d orbitals up to closing the energy gap U at a critical doping content. This corresponds to the insulator to metal transition point which renders the 3d electrons highly delocalized, so that metallic properties emerge.

It stands to reason that metallic properties enhance the hole accumulation and transfer properties of WOCs due to (a) enhanced hole mobility across the bulk of the WOC and (b) faster interface hole transfer from $[\text{Ru}(\text{bpy})_3]^{3+}$ to the WOC through realignment of the valence band. Moreover, the stronger affinity between the metallic compounds and surface oxygen species, as evident from O 1s XPS spectra, is likely to stabilize intermediate oxygen species during water oxidation and to facilitate the interface electron exchange between WOC and the oxygen species as well as the subsequent O—O bond formation. Thus, the major roles of the WOC are strengthened by the metallic band structure, which consistently explains the improved water oxidation activity upon the insulator to metal transition.

CONCLUSIONS

The electronic properties of strongly correlated electronic systems, namely $\text{La}_{1-x}\text{Sr}_x\text{BO}_3$ perovskites and $\text{La}_{2-x}\text{Sr}_x\text{BO}_4$

layered perovskites ($B = \text{Fe}, \text{Co}, \text{Ni}, \text{or Mn}$), were explored for photochemical water oxidation. Gradual substitution of La^{3+} by Sr^{2+} leads to an insulator to metal transition which goes hand in hand with the significant enhancement of water oxidation activity. This introduces metallic properties as a promising design parameter for water oxidation catalyst construction. Strongly correlated electron systems excel through a versatile and easily accessible set of electronic properties, such as localized 3d electrons and orbital ordering. This toolbox of electronic structures can be selectively tuned toward targeted interactions with surface adsorbed molecular species, e.g., interface electron exchange and stabilization of intermediate species. These new perspectives render strongly correlated electron systems promising for the systematic exploration of electronic structure–activity relations in heterogeneous catalysis.

EXPERIMENTAL SECTION

Sample Preparation. All samples were synthesized via a conventional sol–gel method as follows: 6 mmol of the respective metal nitrate salts in the required stoichiometric ratio, 24 mmol citric acid and 3 mL glycol were dissolved in 200 mL deionized water. The as-prepared solution was stirred and condensed at 90°C into a gel which was further decomposed at 180°C for 5 h to form a foam-like precursor. This precursor was subjected to subsequent calcinations ($650^\circ\text{C} + 5\text{ h}$ for $\text{La}_{1-x}\text{Sr}_x\text{BO}_3$ ($B = \text{Fe}, \text{Co}, \text{and Mn}$) and $900^\circ\text{C} + 2\text{ h}$ for $\text{La}_{2-x}\text{Sr}_x\text{BO}_4$ ($B = \text{Co}, \text{Ni}$) in air atmosphere to obtain the final products. $\text{La}_{1-x}\text{Sr}_x\text{CoO}_3$ was reground and subjected to a second calcination ($650^\circ\text{C} + 5\text{ h}$) in pure oxygen atmosphere to improve the phase purity. The ramp rate for all calcinations was set as $5^\circ\text{C}/\text{min}$, and the samples were naturally cooled down to room temperature in the oven after calcination.

Photochemical Water Oxidation. Tests were conducted according to a well-established $[\text{Ru}(\text{bpy})_3]^{2+}/\text{S}_2\text{O}_8^{2-}$ protocol. First, a suspension was prepared by ultrasonic dispersion of the water oxidation catalyst, $[\text{Ru}(\text{bpy})_3]\text{Cl}_2$ (Sigma-Aldrich, 99.95%) photosensitizer and $\text{Na}_2\text{S}_2\text{O}_8$ (Sigma-Aldrich, $\geq 99.0\%$) in 8 mL buffer in a 10 mL vial. Next, the suspension was degassed with helium to remove O_2 in both solution and the head vial in the dark. An LED lamp (460 nm wavelength) with tunable intensity was used as visible light source. Oxygen produced in solution was monitored online with a calibrated Clark electrode (Unisense) and the oxygen diffused to the headspace was detected by gas chromatography (Agilent 7820A packed with a $3\text{ m} \times 2\text{ mm}$ molecular sieve 13X 80–100 column) as follows: 100 μL samples of gas from the head vial were injected into a gas chromatograph using a gastight microliter syringe (Hamilton 1825 RN) during intervals of several minutes. Helium was chosen as carrier gas to increase the detection sensitivity of O_2 . Gases were detected with a thermal conductivity detector (Varian) operated at 200°C . Oxygen contamination by air was subtracted according to N_2 peak area.

Characterization. Powder X-ray diffraction patterns (PXRD patterns) were recorded on a STOE STADI P diffractometer (reflection mode, step size: $0.3^\circ/\text{step}$, $60\text{ s}/\text{step}$) with $\text{Mo K}_{\alpha 1}$ radiation. Fourier transformed infrared (FT-IR) spectra were collected on a Bruker Opus spectrometer at room temperature. XPS spectra were measured on Thermo ESCALAB 250 with a monochromatic Al K_{α} as X-ray source. The C 1s peak at 284.6 eV was set as the reference for all XPS peak position calibrations. Prior to XPS measurements, all samples were dried overnight at 80°C in a drying oven. Magnetization measurements were conducted on a 7 T Quantum Design MPMS XL SQUID at a magnetic field of 1.0 T in the temperature range 2–300 K in both zero field and field cooling modes. The mass susceptibility was calculated according to $\chi = M/(H \cdot m)$ (M : magnetization, H : field strength, m : sample mass). Fe K-edge X-ray absorption spectroscopy (XAS) was performed at the ESRF beamline. $\text{La}_{1-x}\text{Sr}_x\text{FeO}_3$ samples were measured as solid samples dispersed in cellulose in transmission mode. For all experiments, an iron metal foil was used as calibration

standard. Energy calibration, background removal, and Fourier transformation of XAS spectra were performed with the Athena software and EXAFS fits were performed with the Artemis software.⁶⁷

■ ASSOCIATED CONTENT

■ Supporting Information

The Supporting Information is available free of charge on the ACS Publications website at DOI: 10.1021/jacs.5b10215.

Experimental details, additional water oxidation tests and XPS valence band spectra of $\text{La}_{1-x}\text{Sr}_x\text{FeO}_3$, catalytic results and corresponding spectroscopic characterizations of $\text{La}_{1-x}\text{Sr}_x\text{MnO}_3$, $\text{La}_{2-x}\text{Sr}_x\text{NiO}_4$ and $\text{La}_{2-x}\text{Sr}_x\text{CoO}_4$, Rietveld refinements and SEM images of $\text{La}_{1-x}\text{Sr}_x\text{MO}_3$ ($M = \text{Fe}, \text{Co}, \text{and Mn}$), electrochemical tests with $\text{La}_{1-x}\text{Sr}_x\text{CoO}_3$ and spectroscopic characterizations and TEM images of $\text{La}_{0.6}\text{Sr}_{0.4}\text{CoO}_3$ before and after water oxidation are included in the Supporting Information (PDF)

■ AUTHOR INFORMATION

Corresponding Author

*greta.patzke@chem.uzh.ch

Notes

The authors declare no competing financial interest.

■ ACKNOWLEDGMENTS

Financial support by the Swiss National Science Foundation (Sinergia Grant No. CRSII2_136205/1) is gratefully acknowledged. This work has been supported by the University Research Priority Program (URPP) for solar light to chemical energy conversion (LightChEC). H.L. thanks the China Scholarship Council for a PhD fellowship. We thank Dr. Ferdinand Wild (UZH) for ICP-MS measurements and Dr. Hermann Emerich (ESRF Grenoble) for beamline support.

■ REFERENCES

- (1) Walter, M. G.; Warren, E. L.; McKone, J. R.; Boettcher, S. W.; Mi, Q.; Santori, E. A.; Lewis, N. S. *Chem. Rev.* **2010**, *110*, 6446–6473.
- (2) Swierk, J. R.; Mallouk, T. E. *Chem. Soc. Rev.* **2013**, *42*, 2357–2387.
- (3) Lewis, N. S.; Nocera, D. G. *Proc. Natl. Acad. Sci. U. S. A.* **2006**, *103*, 15729–15735.
- (4) Grätzel, M. *Nature* **2001**, *414*, 338–344.
- (5) Gray, H. B. *Nat. Chem.* **2009**, *1*, 7.
- (6) Singh, A.; Spiccia, L. *Coord. Chem. Rev.* **2013**, *257*, 2607–2622.
- (7) Barnett, S. M.; Goldberg, K. I.; Mayer, J. M. *Nat. Chem.* **2012**, *4*, 498–502.
- (8) Yin, Q. S.; Tan, J. M.; Besson, C.; Geletii, Y. V.; Musaev, D. G.; Kuznetsov, A. E.; Luo, Z.; Hardcastle, K. I.; Hill, C. L. *Science* **2010**, *328*, 342–345.
- (9) Fillol, J. L.; Codolà, Z.; Garcia-Bosch, I.; Gomez, L.; Pla, J. J.; Costas, M. *Nat. Chem.* **2011**, *3*, 807–813.
- (10) Brimblecombe, R.; Koo, A.; Dismukes, G. C.; Swiegers, G. F.; Spiccia, L. *J. Am. Chem. Soc.* **2010**, *132*, 2892–2894.
- (11) Sheehan, S. W.; Thomsen, J. M.; Hintermair, U.; Crabtree, R. H.; Brudvig, G. W.; Schmittenmaier, C. A. *Nat. Commun.* **2015**, *6*, 6469.
- (12) Kanan, M. W.; Nocera, D. G. *Science* **2008**, *321*, 1072–1075.
- (13) Jiao, F.; Frei, H. *Angew. Chem., Int. Ed.* **2009**, *48*, 1841–1844.
- (14) Lu, Z.; Wang, H.; Kong, D.; Yan, K.; Hsu, P.-C.; Zheng, G.; Yao, H.; Liang, Z.; Sun, X.; Cui, Y. *Nat. Commun.* **2014**, *5*, 4345.
- (15) Smith, R. D. L.; Prévot, M. S.; Fagan, R. D.; Zhang, Z.; Sedach, P. A.; Siu, M. K. J.; Trudel, S.; Berlinguette, C. P. *Science* **2013**, *340*, 60–63.

- (16) Hocking, R. K.; Brimblecombe, R.; Chang, L.-Y.; Singh, A.; Cheah, M. H.; Glover, C.; Casey, W. H.; Spiccia, L. *Nat. Chem.* **2011**, *3*, 461–466.
- (17) Xu, X.; Random, C.; Efstathiou, P.; Irvine, J. T. S. *Nat. Mater.* **2012**, *11*, 595–598.
- (18) Pokhrel, R.; Goetz, M. K.; Shaner, S. E.; Wu, X.; Stahl, S. S. *J. Am. Chem. Soc.* **2015**, *137*, 8384–8387.
- (19) Pintado, S.; Goberna-Ferrón, S.; Escudero-Adán, E. C.; Galán-Mascarós, J.-R. *J. Am. Chem. Soc.* **2013**, *135*, 13270–13273.
- (20) Cobo, S.; Heidkamp, J.; Jacques, P.-A.; Fize, J.; Fourmond, V.; Guetaz, L.; Jousset, B.; Ivanova, V.; Dau, H.; Palacin, S.; Fontecave, M.; Artero, V. *Nat. Mater.* **2012**, *11*, 802–807.
- (21) Wang, H.; Lee, H.-W.; Deng, Y.; Lu, Z.; Hsu, P.-C.; Liu, Y.; Lin, D.; Cui, Y. *Nat. Commun.* **2015**, *6*, 7261.
- (22) Zhang, M.; Respinis, M.; de Frei, H. *Nat. Chem.* **2014**, *6*, 362–367.
- (23) Gorlin, Y.; Lassalle-Kaiser, B.; Benck, J. D.; Gul, S.; Webb, S. M.; Yachandra, V. K.; Yano, J.; Jaramillo, T. F. *J. Am. Chem. Soc.* **2013**, *135*, 8525–8534.
- (24) Kanan, M. W.; Yano, J.; Surendranath, Y.; Dincă, M.; Yachandra, V. K.; Nocera, D. G. *J. Am. Chem. Soc.* **2010**, *132*, 13692–13701.
- (25) Risch, M.; Ringleb, F.; Kohlhoff, M.; Bogdanoff, P.; Chernev, P.; Zaharieva, I.; Dau, H. *Energy Environ. Sci.* **2015**, *8*, 661–674.
- (26) Park, J.; Kim, H.; Jin, K.; Lee, B. J.; Park, Y.-S.; Kim, H.; Park, I.; Yang, K. D.; Jeong, H.-Y.; Kim, J.; Hong, K. T.; Jang, H. W.; Kang, K.; Nam, K. T. *J. Am. Chem. Soc.* **2014**, *136*, 4201–4211.
- (27) Subbaraman, R.; Tripkovic, D.; Chang, K.-C.; Strmcnik, D.; Paulikas, P. A.; Hirunsit, P.; Chan, M.; Greeley, J.; Stamenkovic, V.; Markovic, N. M. *Nat. Mater.* **2012**, *11*, 550–557.
- (28) Suntivich, J.; May, K. J.; Gasteiger, H. A.; Goodenough, J. B.; Shao-Horn, Y. *Science* **2011**, *334*, 1383–1385.
- (29) Rossmeisl, J.; Qu, Z. W.; Zhu, H.; Kroes, G. J.; Nørskov, J. K. *J. Electroanal. Chem.* **2007**, *607*, 83–89.
- (30) Grimaud, A.; May, K. J.; Carlton, C. E.; Lee, Y.-L.; Risch, M.; Hong, W. T.; Zhou, J.; Shao-Horn, Y. *Nat. Commun.* **2013**, *4*, 2439.
- (31) Robinson, D. M.; Go, Y. B.; Greenblatt, M.; Dismukes, G. C. *J. Am. Chem. Soc.* **2010**, *132*, 11467–11469.
- (32) Maitra, U.; Naidu, B. S.; Govindaraj, A.; Rao, C. N. R. *Proc. Natl. Acad. Sci. U. S. A.* **2013**, *110*, 11704–11707.
- (33) Maiyalagan, T.; Jarvis, K. A.; Therese, S.; Ferreira, P. J.; Manthiram, A. *Nat. Commun.* **2014**, *5*, 3949.
- (34) Gardner, G. P.; Go, Y. B.; Robinson, D. M.; Smith, P. F.; Hadermann, J.; Abakumov, A.; Greenblatt, M.; Dismukes, G. C. *Angew. Chem., Int. Ed.* **2012**, *51*, 1616–1619.
- (35) Lee, S. W.; Carlton, C.; Risch, M.; Surendranath, Y.; Chen, S.; Furutsuki, S.; Yamada, A.; Nocera, D. G.; Shao-Horn, Y. *J. Am. Chem. Soc.* **2012**, *134*, 16959–16962.
- (36) Liu, Y.; Wang, H.; Lin, D.; Liu, C.; Hsu, P.-C.; Liu, W.; Chen, W.; Cui, Y. *Energy Environ. Sci.* **2015**, *8*, 1719–1724.
- (37) Park, J.; Kim, H.; Jin, K.; Lee, B. J.; Park, Y.-S.; Kim, H.; Park, I.; Yang, K. D.; Jeong, H.-Y.; Kim, J.; Hong, K. T.; Jang, H. W.; Kang, K.; Nam, K. T. *J. Am. Chem. Soc.* **2014**, *136*, 4201–4211.
- (38) Liu, H.; Zhou, Y.; Moré, R.; Müller, R.; Fox, T.; Patzke, G. R. *ACS Catal.* **2015**, *5*, 3791–3800.
- (39) Dagotto, E. *Science* **2005**, *309*, 257–262.
- (40) Selwood, P. W. *Chem. Rev.* **1946**, *38*, 41–82.
- (41) Sivaraja, M.; Philo, J. S.; Lary, J.; Dismukes, G. C. *J. Am. Chem. Soc.* **1989**, *111*, 3221–3225.
- (42) Bhalla, A. S.; Guo, R.; Roy, R. *Mater. Res. Innovations* **2000**, *4*, 3–26.
- (43) Peña, M. A.; Fierro, J. L. G. *Chem. Rev.* **2001**, *101*, 1981–2018.
- (44) Snaith, H. J. *J. Phys. Chem. Lett.* **2013**, *4*, 3623–3630.
- (45) Moure, C.; Peña, O. *Prog. Solid State Chem.* **2015**, *43*, 123.
- (46) King, G.; Woodward, P. M. *J. Mater. Chem.* **2010**, *20*, 5785–5796.
- (47) Eng, H. W.; Barnes, P. W.; Auer, B. M.; Woodward, P. M. *J. Solid State Chem.* **2003**, *175*, 94–109.
- (48) Dann, S. E.; Currie, D. B.; Weller, M. T.; Thomas, M. F.; Al-Rawwas, A. D. *J. Solid State Chem.* **1994**, *109*, 134–144.

- (49) Pokhrel, R.; Goetz, M. K.; Shaner, S. E.; Wu, X.; Stahl, S. S. *J. Am. Chem. Soc.* **2015**, *137*, 8384–8387.
- (50) Tajima, S.; Masaki, A.; Uchida, S.; Matsuura, T.; Fueki, K.; Sugai, S. *J. Phys. C: Solid State Phys.* **1987**, *20*, 3469–3484.
- (51) Haas, O.; Vogt, U. F.; Soltmann, C.; Braun, A.; Yoon, W.-S.; Yang, X. Q.; Graule, T. *Mater. Res. Bull.* **2009**, *44*, 1397–1404.
- (52) Sardar, K.; Petruccio, E.; Hiley, C. I.; Sharman, J. B. D.; Wells, P. P.; Russell, A. E.; Kashtiban, R. J.; Sloan, J.; Walton, R. I. *Angew. Chem., Int. Ed.* **2014**, *53*, 10960–10964.
- (53) Adler, S. B.; Chen, X. Y.; Wilson, J. R. *J. Catal.* **2007**, *245*, 91–109.
- (54) Fujimori, A.; Mizokawa, T.; Saitoh, T.; Namatame, H. *Phys. Rev. B: Condens. Matter Mater. Phys.* **1992**, *45*, 1561–1570.
- (55) Ramaker, D. E.; Turner, N. H.; Murday, J. S. *Phys. Rev. B: Condens. Matter Mater. Phys.* **1987**, *36*, 5672–5675.
- (56) Blasco, J.; Aznar, B.; García, J.; Subías, G.; Herrero-Martín, J.; Stankiewicz, J. *Phys. Rev. B: Condens. Matter Mater. Phys.* **2008**, *77*, 054107.
- (57) Fossdal, A.; Menon, M.; Wærnhus, I.; Wiik, K.; Einarsrud, M.-A.; Grande, T. *J. Am. Ceram. Soc.* **2004**, *87*, 1952–1958.
- (58) Risch, M.; Grimaud, A.; May, K. J.; Stoerzinger, K. A.; Chen, T. J.; Mansour, A. N.; Shao-Horn, Y. *J. Phys. Chem. C* **2013**, *117*, 8628–8635.
- (59) May, K. J.; Carlton, C. E.; Stoerzinger, K. A.; Risch, M.; Suntivich, J.; Lee, Y.-L.; Grimaud, A.; Shao-Horn, Y. *J. Phys. Chem. Lett.* **2012**, *3*, 3264–3270.
- (60) Mineshige, A.; Inaba, M.; Yao, T.; Ogumi, Z. *J. Solid State Chem.* **1996**, *121*, 423–429.
- (61) Sudheendra, L.; Seikh, M. M.; Raju, A. R.; Narayana, C. *Chem. Phys. Lett.* **2001**, *340*, 275–281.
- (62) Kozuka, H.; Yamada, H.; Hishida, T.; Yamagiwa, K.; Ohbayashi, K.; Koumoto, K. *J. Mater. Chem.* **2012**, *22*, 20217–20222.
- (63) Gorlin, Y.; Lassalle-Kaiser, B.; Benck, J. D.; Gul, S.; Webb, S. M.; Yachandra, V. K.; Yano, J.; Jaramillo, T. F. *J. Am. Chem. Soc.* **2013**, *135*, 8525–8534.
- (64) Risch, M.; Ringleb, F.; Kohlhoff, M.; Bogdanoff, P.; Chernev, P.; Zaharieva, I.; Dau, H. *Energy Environ. Sci.* **2015**, *8*, 661–674.
- (65) Kanan, M. W.; Yano, J.; Surendranath, Y.; Dincă, M.; Yachandra, V. K.; Nocera, D. G. *J. Am. Chem. Soc.* **2010**, *132*, 13692–13701.
- (66) Hemberger, J.; Krimmel, A.; Kurz, T.; Krug von Nidda, H.-A.; Ivanov, V. Y.; Mukhin, A. A.; Balbashov, A. M.; Loidl, A. *Phys. Rev. B: Condens. Matter Mater. Phys.* **2002**, *66*, 094410.
- (67) Ravel, B.; Newville, M. *J. Synchrotron Radiat.* **2005**, *12*, 537.